Optics Letters

Sub-second, super-resolved imaging of biological systems using parallel EO-STED

Arik Girsault and Amit Meller*

Department of Biomedical Engineering, Technion—IIT, Haifa 32000, Israel
**Corresponding author: ameller@technion.ac.il*

Received 16 March 2020; accepted 6 April 2020; posted 8 April 2020 (Doc. ID 392822); published 6 May 2020

We present a parallel stimulated emission depletion (STED) nanoscope with no mechanical moving parts and sub-millisecond pixel dwell times, relying on electro-optical (EO) phase modulators. The nanoscope offers 1225-fold parallelization over single-doughnut-scanning STED and achieves a spatial resolution of 35 nm. We imaged immunostained nuclear pore complexes of zebrafish within their natural biological environment, demonstrating spatial and temporal resolutions of 56 nm and 0.2 s, respectively. Furthermore, we show parallel EO-STED sub-second imaging of microtubules inside living cells. Finally, we reveal the nanodomain organization of a eukaryotic initiation factor within the processing bodies of fixed cells. The potential of parallel EO-STED to offer microsecond pixel dwell times over large fields of view promises millisecond STED imaging.

https://doi.org/10.1364/OL.392822

The advent of super-resolution imaging modalities [1,2], which overcome the optical diffraction limit by exploiting the photophysical properties of fluorescent molecules, has led to optical imaging at the nanoscale level of a plethora of biological specimens. Stimulated emission depletion (STED) microscopy is a prominent example of such an imaging technique and has seen tremendous improvements over the past decade, giving rise to increasing spatial and temporal resolutions, as well as an improved compatibility with biological specimens [3]. STED and its variants [4] are almost invariably implemented as point-scanning techniques, creating an inherent conflict between the short pixel dwell time required for full image acquisition and photon budget per pixel [5,6]. Consequently, to date, due to the necessary pixel-wise scanning, high imaging speeds have only been achieved for densely labeled specimens, relatively low spatial resolutions, and rather small fields of view [3,7]. Specifically, spatial resolutions of 40–60 nm often entail an image acquisition in the order of tens of seconds or more, which is several orders of magnitude slower than many of the sought-after biomolecular processes [8–10]. Furthermore, fast point-scanning typically necessitates high repetition rate lasers (20–80 MHz), which have the side effect of promoting photobleaching and phototoxicity [11–13]. To address these limitations, approaches aiming at parallelizing STED microscopy—collectively referred to as *parallel STED* microscopy—were developed [4].

Parallel STED was first introduced as the multiplexing of four cloned STED point spread functions (PSFs) and corresponding point detectors [14], thus achieving a four-fold parallelization. Consequently, upscaling such a system either for imaging spectrally distinct fluorophores or for increasing the degree of parallelization would significantly increase its complexity. As an alternative, the conjunction of two orthogonal standing waves for producing the STED inhibition pattern and of wide-field illumination for the excitation pattern, in designs analogous to that of parallel reversible saturable optical fluorescence transitions (RESOLFT) microscopy [15,16], has shown to be a very promising concept. With the original optical design [17], a 100-fold parallelization was achieved over a rather small field of view (3 μm × 3 μm) and an impressive 2000-fold parallelization at a spatial resolution of ∼55 nm over a field of view of ∼20 μm by 20 μm with another [18]. The largest degree of parallelization attained so far was 13,000 over a field of view of 34 μm by 34 μm based on an optical design that uses diffraction gratings for generating the depletion fringes [19]. In addition, these latter interference-based parallel STED methods require five-fold less average power to achieve a spatial resolution comparable to that of point-scanning STED microscopy and allow further reduction of the laser repetition rate, both of which contribute significantly to reducing photobleaching and phototoxicity while increasing the fluorescence yield. In a recent computational study, Xue *et al.* have also provided a theoretical basis on which to build a three-dimensional parallel STED imaging modality using spatial light modulators [20].

Nonetheless, current implementations and designs of parallel STED do not reflect the fastest acquisition speed one could achieve with a given level of parallelization and camera frame rate. Indeed, the STED pattern-scanning unit, which typically relies on scanning mirrors, increases the acquisition time of each scanned pixel array by at least 3 to 8 ms regardless of the camera acquisition rate and the emitted photon flux. To address this limitation, we have developed another variant of parallel STED microscopy, i.e., parallel electro-optical (EO) STED, which, though for the most part is identical to the approach presented in Ref. [18], does not involve any moving elements, and instead relies on phase-shifting EO modulators (EOMs) for image acquisition. This allows, in principle, a faster acquisition of an image as compared with mirror scanning, although, with

the present imaging devices, the camera frame rates remain a limiting factor.

A schematic of the parallel EO-STED is shown in Fig. 1. The pulsed STED laser (775 nm, 0.7–0.9 ns, Katana-08HP, OneFive) delivers an average power of 2 W at 2 MHz. The STED beam is expanded to a final size of approximately 2 mm by a telescope. The optical path also includes an acousto-optic modulator (AOM, MTS40-A3-750,850 AA Opto-Electronics) for sub-microsecond (μs) on–off switching of the STED beam, thus preventing unnecessary exposure during either readout or in between super-resolved frames. A first variable polarizing beam splitter (WPH05M-780 Thorlabs, PBS25-780 Thorlabs) splits the STED light into two orthogonally polarized beams with equal energies and redirects each towards a two-arm Michelson-like interferometer. Figure 1 depicts the polarization state of the four STED beams as they propagate through their respective interferometer arms and as they merge with one polarizing beam splitter placed downstream of the optical path. All four beams subsequently pass through a 2-mm-thick dichroic filter (FF765-Di01, Semrock) and are directed at the focal plane of the objective lens (Plan-APO 100 × NA1.46 Oil, Zeiss), at which they interfere to produce the STED depletion fringes. The interference angle on the sample plane approaches $\pi/3$, thus resulting in an overall parallelization of ∼1225 over a 10.6 μm × 10.6 μm field of view and a 9.7-fold energy efficiency over conventional doughnut-scanning STED [18]. The fringes are scanned over a unit cell—the area delimited by four neighboring zeros—through stepwise phase delays introduced between the arms of each interferometer using the EO phase modulators (EO-PM-NR-C1, Thorlabs), as shown in Fig. 1.

A laser diode (LDH-D-C 640, Picoquant), which could either be operated in pulsed (80–100 ps) or continuous-wave mode, was used as a 638 nm excitation source. The beam was first cleaned using a single-mode, polarization-preserving, optical fiber (>55% transmission efficiency) and subsequently expanded to the desired waist diameter by a telescope. The excitation beam is then guided towards the objective lens, reflecting off both the dichroic filter separating excitation from emission (zt440/488/561/635rpc-UF2, Chroma) and the one (FF765-Di01, Semrock) merging the STED and excitation beam. The emitted fluorescence signals are observed over a 650–700 nm spectral region using a bandpass filter (676/37 nm BrightLine, Semrock) and subsequently imaged on an electron-multiplying charged coupled device (EMCCD) camera (iXon+ 860, Andor). A camera pixel corresponds to an 83 nm × 83 nm area in the sample plane. Data acquisition is performed by a custom program, which synchronizes the camera with the gating mechanisms of the excitation laser (using the fast-gating operation of the Picoquant controller) and the STED laser via the AOM, as well as the voltage steps applied to the EOMs for scanning the fringes on the sample plane.

The image analysis procedure applied to the stack of images recorded during a parallel EO-STED acquisition consists of three steps. (1) The rotation angles and periods of the fringes are estimated using the chirp Z transform (CZT)—a generalization of the discrete Fourier transform (DFT) used here as an implementation of the 'zoom DFT'. Briefly, we first apply the CZT to each image of the acquired stack over a coarse spatial-frequency range centered on the zeroth frequency. The moduli of the subsequent CZT images are then summed, and the modulus of the CZT of the summed image stack (i.e., the

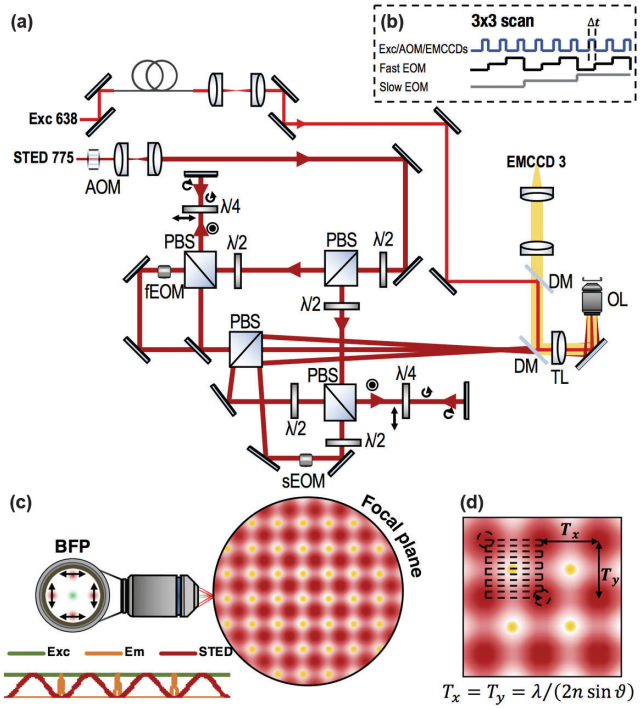

Fig. 1. Parallel EO-STED optical design and principles. (a) Schematics of the parallel EO-STED. (b) Sequence of voltage pulses and steps synchronizing acquisition, excitation, depletion, and scanning. (c) Four STED spots equidistant to the optical axis (green excitation) are focused on the objective pupil plane. As a result, the sample is illuminated by wide-field excitation and four collimated depletion beams propagating at an angle θ with respect to the optical axis: two-beam interference occurs, one emerging from a pair of vertically polarized (x-interference fringes) and the other from a pair of horizontally polarized (y-interference fringes) beams. Superposition of y- and x-interference fringes leads to the 2D parallel STED depletion pattern whose spacing in y and x is defined by T_y and T_x, respectively. Fluorescence signals (shown in yellow) are confined at the fringes' zeros. (d) The STED pattern is scanned in y (and x) by delaying either one of the two horizontally (or vertically) polarized beams with respect to one another using an electro-optics phase modulator. Exc, excitation laser; EMCCD, electron-multiplying charged coupled device; SMF, single-mode fiber; DM, dichroic mirror; AOM, acousto-optics modulator; $\lambda/4$, quarter-wave plate; $\lambda/2$, half-wave plate; PBS, polarizing beam splitter; fEOM, fast-scanning electro-optics modulator; sEOM, slow-scanning electro-optics modulator; TL, tube lens; and OL, objective lens.

wide-field image) is subtracted. This allows us to emphasize in the resulting CZT image the peaks stemming from the two-dimensional (2D) fringes. We then repeat the same procedure four times, i.e., once for each peak (over a spatial-frequency range centered on its location). The locations of the peaks are determined and used to calculate the periods (distance from the origin to the locations), as well as the rotation angles (the vertical or horizontal angles between an axis and the line joining the pair of corresponding peaks). By observing the phase difference between successive CZT images at the determined peaks' locations, one can also estimate the scanning step size. The phase offsets are subsequently estimated by correlating simulated fringes with the acquired image stack. (2) The parallel STED pixel values are determined separately for each acquired frame

by integrating PSFs centered at the grid points, i.e., located at the zero-intensity regions of the depletion pattern. The crosstalk between the neighboring STED pixels of each grid is removed in a linear matrix operation, as described in detail in Ref. [19]. Finally, (3) the super-resolved image is assembled from the STED pixel grids to which is subtracted a scaled wide-field image as a background reduction method. The half-wave EOM voltage, with which the scanning step size on the sample is determined, was computed beforehand using fluorescent beads; the previously described estimation algorithm and visual feedback are based on the quality of the assembled STED image.

To investigate the spatial resolution of the parallel EO-STED imaging, we used fluorescently labeled nanorulers immobilized on a glass coverslip (GATTA-STED50R, Gattaquant). The rulers carried two fluorescent marks separated by 50 nm. Each of the fluorescent marks is made of a dense arrangement of ~15 Atto647N dyes. We imaged an area of 10.6 μm × 10.6 μm in the sample (Fig. 2). The 2D depletion fringes were scanned using a depletion laser power of ~0.9 W, on a 22 × 22 grid, leading to an ~15 nm pixel size. The measured full width at half-maximum (FWHM) of single fluorescent marks with these settings was 44 ± 4 nm [Fig. 2(c)], and the mark-to-mark distance was 47 ± 10 nm [Fig. 2(d)], showing good agreement with the ruler specifications. Further increasing the STED laser power to determine the highest achievable resolution led to slight bleaching of the fluorophores in the course of scanning, though the FWHM and the mark-to-mark distance measured in this case from 10 nanorulers in the center region was 35.8 ± 3 nm and 49.8 ± 4 nm, respectively. Next, in order to demonstrate the scanning capabilities of parallel EO-STED, we imaged 23 nm fluorescent beads (GATTA-Beads R, Gattaquant) over a restricted field of view of 2.1 μm × 8.6 μm to achieve a corresponding camera frame rate of ~1110/s, i.e., sub-millisecond pixel dwell times [Fig. 2(e)]. This constitutes an improvement of an order of magnitude over the acquisition frame rates reported in interference-based parallel STED [19]. The plotted profiles [Fig. 2(f)] demonstrate a spatial resolution of 46 ± 11 nm, even at such high speeds, and low excitation laser powers.

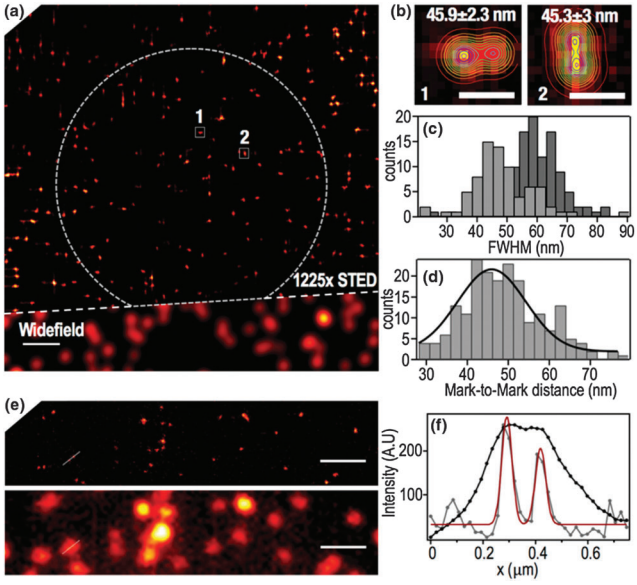

Fig. 2. Parallel EO-STED imaging of nanorulers and nanobeads. (a) 1225-fold parallelized STED versus wide-field image of nanorulers. (b) Magnified regions of two orthogonal nanorulers fitted with Gaussian functions. The FWHM of the fits is shown in each inlet. (c) Histograms of the FWHM values fitted to the nanorulers of the STED image. The light gray histogram considers nanorulers within the central region of the STED image—delimited by the circular dashed line in (a)—and the dark gray histogram considers the nanorulers of the remaining peripheral region. (d) Histogram of the nanoruler mark-to-mark distance fit values of the STED image. (e) Parallel EO-STED versus wide-field image of nanobeads acquired in 200 ms. (f) Intensity profile plots across two nanobeads at gray line in (e) overlaid with a Gaussian fit of the STED profile (red line). Scale bars in (a) and (e) 1 μm, (b) 80 nm.

We demonstrate the capabilities of parallel EO-STED by imaging living U2OS cells labeled with silicon rhodamine (SiR)-Tubulin [21], a cell permeable SiR dye specific for microtubules [Fig. 3(a)–3(c)]. The cells were imaged in an imaging chamber (UNO-T-H-CO2, Okolab; H301-MCL-Z100/500, Mad City Labs) in which temperature, humidity, and CO_2 levels were set to 37°C, 90%, and 5%, respectively. The full field of view was acquired in <1 s and the FWHM of the measured profile across several filaments ranged from 95 to 150 nm [Fig. 3(b)]. We noted that a microtubule whose kinetics is faster than that of the acquisition speed would appear undulated in the final reconstructed STED image, as expected in a parallelized acquisition scheme. Finally, we also show that the spatial resolution improvement gained in live cell parallel EO-STED disentangled microtubules, which were otherwise indistinguishable from one another in the wide-field image [Fig. 3(c)].

In addition, we used parallel EO-STED to image in fixed U2OS cells the organization of a key regulator of cap-dependent translation initiation (eIF4E) within processing (P) bodies. A

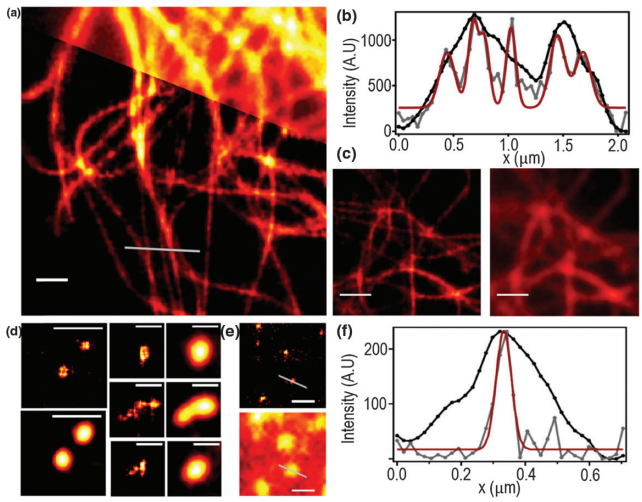

Fig. 3. Parallel EO-STED imaging of biological specimens. (a) Parallel EO-STED imaging of microtubules labeled with silicon rhodamine (SiR). (b) Intensity line profile plots across microtubules at the gray line in (a) overlaid with a Gaussian fit of the STED profile (dark red line). (c) Parallel EO-STED versus wide-field imaging of SiR-labeled microtubules. (d) Parallel EO-STED imaging of eIF4E nanodomains immunolabeled with Atto647N in fixed U2OS cells. (e) Parallel EO-STED imaging of nuclear pore complexes in a fixed zebrafish tail. (f) Intensity profile plots across a nuclear pore at the gray line in (e) overlaid with a Gaussian fit of the STED profile (dark red line). Scale bars in (a), (c), and left column of (d) 1 μm; in right columns of (d) and (e) 0.5 μm.

spatial resolution of ∼45 nm revealed an arrangement of 'nanodomains', ranging in sizes from 50 to 80 nm approximately [Fig. 3(d)]. This organization would likely be reflected in the dynamics of eIF4E release or sequestration into P-bodies and thus of post-translational regulation.

Finally, we characterized the performance of parallel EO-STED by imaging fixed eukaryotic cells from zebrafish. These samples are transparent at early stages and genetically tractable vertebrates, which have proven to be useful models for regulatory physiology, developmental biology, and more recently neurosciences [22]. We imaged the cellular nuclear pore complexes of a fixed zebrafish tail immunolabeled by MAb414 with Atto647N [Fig. 3(e)–3(f)]. The 2D depletion fringes were scanned on 15×15 grid, and a restricted field of view ($3.0\ \mu m \times 10.6\ \mu m$) was acquired in ∼0.2 s, corresponding to 900 µs pixel dwell times. A sub-region in which several pores were super-resolved in a single focal plane is shown in Fig. 3(e). The profile plot of the STED image [Fig. 3(f)] was fitted to a Gaussian function, demonstrating a spatial resolution of 56 ± 10 nm.

To summarize, we have presented a new variant of parallel STED microscopy, based on an ultrafast scanning scheme that does not involve any mechanical moving part, thereby improving its potential temporal resolution by several orders of magnitude. With the advent of single-photon avalanche diode (SPAD) arrays for imaging [23,24], the camera frame rates may not be the main limiting factor on parallel STED speed. In such cases, EOM scanning can offer a significant advantage over mechanical scanning approaches, allowing us to advance our ability towards fast image acquisition in parallel STED nanoscopy; especially considering that pixel dwell times of only a few µs are consistently used in STED microscopy and are even progressively entering the nanosecond regime [4].

It is noteworthy that the optical design of parallel EO-STED is compatible with stochastic optical reconstruction microscopy (STORM) [25]. As a consequence, using parallel EO-STED, the researcher will operate a single versatile tool with which he can investigate various biological systems labeled with qualitatively different dyes (whether optimized for photostability, photoblinking kinetics, brightness, photoactivability, and so on). By tuning the intensity, number of scanning steps, and exposure time, the 2D depletion fringes essentially produce an image stack of emitters blinking at an arbitrary frequency, which can also (in addition to the parallel EO-STED algorithm) be analyzed by stochastic super-resolution techniques. This confers not only the advantage of generating super-resolved images without having to estimate the period, phase offset, and scanning step of the STED fringes [18] but also of providing additional features offered by these typical stochastic methods, such as background suppression in super-resolution optical fluctuation imaging (SOFI) [26].

Funding. Wolfson Foundation; National Cancer Institute (R01CA202021).

Acknowledgment. We thank Dr. Limor Freifeld for the immunolabeled zebrafish tails, Dr. Diana Huttner for the fixed and live U2OS cells sample preparation, and Adam Zrehen for developing the LabVIEW-based control software.

Disclosures. The authors declare no conflicts of interest.

REFERENCES

1. S. J. Sahl, A. Schönle, and S. W. Hell, *Springer Handbook of Microscopy* (Springer, 2019), p. 2.
2. L. Schermelleh, A. Ferrand, T. Huser, C. Eggeling, M. Sauer, O. Biehlmaier, and G. P. C. Drummen, Nat. Cell Biol. **21**, 72 (2019).
3. S. J. Sahl and S. W. Hell, *High Resolution Imaging in Microscopy and Ophthalmology* (Springer, 2019), pp. 3–32.
4. G. Vicidomini, P. Bianchini, and A. Diaspro, Nat. Methods **15**, 173 (2018).
5. S. Galiani, B. Harke, G. Vicidomini, G. Lignani, F. Benfenati, A. Diaspro, and P. Bianchini, Opt. Express **20**, 7362 (2012).
6. L. Lanzanò, L. Scipioni, M. Castello, P. Bianchini, G. Vicidomini, and A. Diaspro, *Springer Series on Fluorescence* (Springer, 2016), Chap. 19, pp. 311–329.
7. H. Blom and J. Widengren, Curr. Opin. Chem. Biol. **20**, 127 (2014).
8. J. Howard and R. Clark, Appl. Mech. Rev. **55**, B39 (2002).
9. C. Wang, B. Han, R. Zhou, and X. Zhuang, Cell **165**, 990 (2016).
10. S. Mochida, Proc. Jpn. Acad. **93**, 802 (2017).
11. X. Nan, E. O. Potma, and X. S. Xie, Biophys. J. **91**, 728 (2006).
12. G. Donnert, J. Keller, R. Medda, M. A. Andrei, S. O. Rizzoli, R. Luhrmann, R. Jahn, C. Eggeling, and S. W. Hell, Proc. Natl. Acad. Sci. USA **103**, 11440 (2006).
13. J. Oracz, V. Westphal, C. Radzewicz, S. J. Sahl, and S. W. Hell, Sci. Rep. **7**, 11354 (2017).
14. P. Bingen, M. Reuss, J. Engelhardt, and S. W. Hell, Opt. Express **19**, 23716 (2011).
15. A. Chmyrov, J. Keller, T. Grotjohann, M. Ratz, E. D'Este, S. Jakobs, C. Eggeling, and S. W. Hell, Nat. Methods **10**, 737 (2013).
16. A. Chmyrov, M. Leutenegger, T. Grotjohann, A. Schönle, J. Keller-Findeisen, L. Kastrup, S. Jakobs, G. Donnert, S. J. Sahl, and S. W. Hell, Sci. Rep. **7**, 44619 (2017).
17. B. Yang, F. Przybilla, M. Mestre, J.-B. Trebbia, and B. Lounis, Opt. Express **22**, 5581 (2014).
18. F. Bergermann, L. Alber, S. J. Sahl, J. Engelhardt, and S. W. Hell, Opt. Express **23**, 211 (2015).
19. F. Bergermann, "Massively parallelized STED nanoscopy," Ph.D. thesis (Ruperto-Carola University of Heidelberg, 2016).
20. Y. Xue and P. T. C. So, Opt. Express **26**, 20920 (2018).
21. G. Lukinavičius, K. Umezawa, N. Olivier, A. Honigmann, G. Yang, T. Plass, V. Mueller, L. Reymond, I. R. Corrêa, Z.-G. Luo, C. Schultz, E. A. Lemke, P. Heppenstall, C. Eggeling, S. Manley, and K. Johnsson, Nat. Chem. **5**, 132 (2013).
22. J. P. Briggs, Am. J. Physiol. **282**, R3 (2002).
23. D. Bronzi, F. Villa, S. Tisa, A. Tosi, F. Zappa, D. Durini, S. Weyers, and W. Brockherde, IEEE J. Sel. Top. Quantum Electron. **20**, 354 (2014).
24. I. M. Antolovic, S. Burri, C. Bruschini, R. Hoebe, and E. Charbon, IEEE Trans. Electron Devices **63**, 57 (2016).
25. M. J. Rust, M. Bates, and X. Zhuang, Nat. Methods **3**, 793 (2006).
26. T. Dertinger, R. Colyer, G. Iyer, S. Weiss, and J. Enderlein, Proc. Natl. Acad. Sci. USA **106**, 22287 (2009).